In-flight measurement of atmospheric-imposed tilt: experimental results and analysis

Matthew Kalensky,[1,*] [ID] **Eric J. Jumper,**[2] **Matthew R. Kemnetz,**[3] **and Stanislav Gordeyev**[2]

[1]*Integrated Engagement Systems Department, Naval Surface Warfare Center Dahlgren Division, Dahlgren, Virginia 22448, USA*
[2]*Aerospace and Mechanical Engineering Department, University of Notre Dame, Notre Dame, Indiana 46556, USA*
[3]*Air Force Research Laboratory, Directed Energy Directorate, Kirtland Air Force Base, New Mexico 87117, USA*
*Corresponding author: mtkalensky@gmail.com

The work presented here experimentally measures the tilt imposed on a laser beam by the atmosphere from Shack–Hartmann wavefront sensor measurements collected in-flight. Tip/tilt is imposed on the laser beam by propagating through optical turbulent structures larger than or of the order of the size of the beam diameter. This tip/tilt causes a dynamic, net deflection of the beam in the far field, referred to as jitter, which poses a serious problem for tracking in directed energy applications. The practical measurement of turbulence-induced tip/tilt at altitude is challenging since mechanical contamination in the form of vibrations also manifests as tip/tilt. In this paper, a procedure referred to as the stitching method is used to quantify the turbulence-induced component of tilt without the influence of mechanical corruption. It is found that the measured tilt aligns with what analytic solutions predict and that the turbulent environment through which the beam propagates has Kolmogorov-like characteristics. © 2022 Optica Publishing Group

1. INTRODUCTION

The index of refraction is related to the air density by the Gladstone–Dale relation

$$n(x, y, z, t) = 1 + K_{GD}(\lambda)\rho(x, y, z, t), \qquad (1)$$

where n is the index of refraction, ρ is the density, and K_{GD} is the Gladstone–Dale constant [1]. When an electromagnetic wave is of a single wavelength, λ, such as in the case of a laser, the wavefront (a surface of constant phase) can lead or lag over the mean wavefront. This occurs if the index of refraction is not uniform over the diameter of the laser beam, D. The distortions imposed on the wavefront resulting from density non-uniformities can be categorized into the mean, tip/tilt[$\theta_y(t)$ and $\theta_x(t)$] components, as well as variations over the laser beam diameter referred to as higher-order disturbances. The higher-order disturbances cause the laser beam to spread energy out in the far field. For distortions of the order of D and larger, tip/tilt is imposed on the beam, causing it to deflect from its original path. Consequently, a beam directed at a distant aim-point is deflected away from that aim-point. To the extent that the density variations in the beams path are moving, this now dynamic net deflection of the beam is referred to as jitter. For the application of airborne mounted beam control systems, beam jitter reduces the ability to maintain the laser beam on the aim-point, significantly reducing system performance. Analytic solutions exist that

describe the relationship between atmospheric optical turbulence strength and the resultant atmospheric tilt [2]. However, to the authors' knowledge, experimental measurements of atmospheric tilt have not been made in flight. The work presented here seeks to measure the atmospheric contribution of tilt imposed on a laser beam that propagates through different atmospheric turbulence environments at altitude.

To make these measurements, the Airborne Aero-Optics Laboratory (AAOL) was used [3–13]. AAOL is an in-flight testing platform consisting of two aircraft capable of flying in formation at varying altitudes and separations. One aircraft, referred to as the "source aircraft," projects a laser beam through the atmosphere to the second aircraft, referred to as the "laboratory aircraft" [9]. The systems installed in both aircraft are equipped with tracking systems such that as they fly through the atmosphere, regardless of turbulence, mechanical vibrations, or aircraft flight path, the laser beam remains engaged with the desired aim-point. In this case, the desired aim-point is the optical acquisition window on the laboratory aircraft. At large aircraft separations, optical disturbances from the atmosphere are imposed on the beam. After the laser beam enters the laboratory aircraft through the acquisition window, the optical distortions imposed on the laser beam are measured using a Shack–Hartmann wavefront sensor (SHWFS). The slopes measured by the SHWFS are converted to wavefronts using a least-squares reconstructor. Using the Zernike definition of tilt

(Z-tilt), tip/tilt can then be quantified from the reconstructed wavefronts. Unfortunately, mechanical contamination also manifests as tip/tilt and until this point, has prohibited the measurement of the atmospheric tip/tilt in-flight without severe contamination from these non-turbulence related disturbances. Due to this mechanical contamination, all tip/tilt and pistons are initially removed from the measured wavefronts in post-processing.

Recently, an approach referred to as the stitching method was developed to reintroduce the turbulence-induced component of tip/tilt and piston into the wavefronts without the influence of mechanical contamination [14,15]. Details of the stitching method are described in the sections to come. After using the stitching algorithm, the power spectral density and root-mean-square values of the atmospheric tilt were computed and compared with analytic predictions.

2. MEASUREMENT OF ATMOSPHERIC-IMPOSED TILT

This section begins by describing how wavefront error and tip/tilt and piston are quantified. Next, the stitching algorithm is described, which allows the turbulence-induced tip/tilt and piston to be reintroduced into the wavefronts without the tip/tilt and piston resulting from mechanical contamination.

A. Quantifying Wavefront Disturbances

Optical path length (OPL) and optical path difference (OPD) are typically used to quantify the severity of aberrations imposed on a laser. OPL is defined as the path integral of the index of refraction:

$$\mathrm{OPL}(x, y, t) = \int_{z_1}^{z_2} n(x, y, z, t) \mathrm{d}z, \qquad (2)$$

where $\hat{z}$ is the propagation path direction [1]. OPD is the result of removing the spatial mean (or piston) from the OPL, given by

$$\mathrm{OPD}(x, y, t) = \mathrm{OPL}(x, y, t) - \overline{\mathrm{OPL}(x, y, t)}. \qquad (3)$$

OPD is often approximated as the conjugate of the wavefront: $\mathrm{OPD}(x, y, t) = -W(x, y, t)$. For simplicity, OPD and W are used interchangeably in this paper. By taking the root-mean-square of $\mathrm{OPD}(x, y, t)$ in space, we get the $\mathrm{OPD_{RMS}}(t)$, which describes the wavefront's time-dependent departure from a flat surface [16]. Furthermore, time averaging yields the $\mathrm{OPD_{RMS}}$, which is a common metric for quantifying the severity of wavefront aberrations. $\mathrm{OPD_{RMS}}$ can be reported for either the overall wavefront disturbances, including tip/tilt and piston, or tip/tilt and piston removed wavefront disturbances.

As described in the Introduction, tip/tilt aberrations, $\theta_y(t)$ and $\theta_x(t)$, result when a laser propagates through optical turbulence structures larger than or of the order of the size of the beam diameter. Since the full spatial structure cannot be resolved within the viewing aperture, these larger structures tend to impose a bulk angular distortion onto the beam. When calculating tip/tilt, there are two definitions prevalent in literature: gradient tilt (G-tilt) and Z-tilt. G-tilt is the result of averaging all local gradients over a wavefront. Z-tilt comes from the first

radial degree terms of the Zernike polynomial expansion. For the purposes of this paper, the Z-tilt definition was used to quantify tilt. To calculate Z-tilt, a least-squares fit is applied to the plane of the wavefront. The error associated with the least-squares fit of the wavefront plane, given by

$$\mathrm{Error}(\theta_x(t), \theta_y(t), C(t))$$

$$= \iint_D (W(x, y, t) - [\theta_x(t)x - \theta_y(t)y + C(t)])^2 \mathrm{d}x\mathrm{d}y, \qquad (4)$$

is minimized by solving a system of linear equations. The resultant coefficients, $\theta_y(t)$, $\theta_x(t)$, and $C(t)$, are the tip, tilt, and piston values, respectively [14,17]. The system of equations to solve for these coefficients is as follows:

$$\begin{bmatrix} \iint_D x^2 \mathrm{d}x\mathrm{d}y & \iint_D xy\,\mathrm{d}x\mathrm{d}y & \iint_D x\,\mathrm{d}x\mathrm{d}y \\ \iint_D xy\,\mathrm{d}x\mathrm{d}y & \iint_D y^2 \mathrm{d}x\mathrm{d}y & \iint_D y\,\mathrm{d}x\mathrm{d}y \\ \iint_D x\,\mathrm{d}x\mathrm{d}y & \iint_D y\,\mathrm{d}x\mathrm{d}y & \iint_D 1\mathrm{d}x\mathrm{d}y \end{bmatrix} \cdot \begin{bmatrix} \theta_x(t) \\ \theta_y(t) \\ C(t) \end{bmatrix}$$

$$= \begin{bmatrix} \iint_D W(x, y, t)x\,\mathrm{d}x\mathrm{d}y \\ \iint_D W(x, y, t)y\,\mathrm{d}x\mathrm{d}y \\ \iint_D W(x, y, t)\mathrm{d}x\mathrm{d}y \end{bmatrix}. \qquad (5)$$

Here, the tip/tilt coefficients as a function of time are "global" tilts. Piston, or the mean component, does not affect the far-field intensity pattern and therefore is not heavily emphasized in this work. Generally speaking, the axes associated with tip and tilt are arbitrary. In this paper, the authors consider "tip," or $\theta_y(t)$, to be associated with angular beam deflections in the "up-down" or cross-stream direction, and "tilt," or $\theta_x(t)$, to be associated with the angular beam deflections in the "left-right" or streamwise direction. The measurement of atmospheric tilt is the primary emphasis of the work presented here.
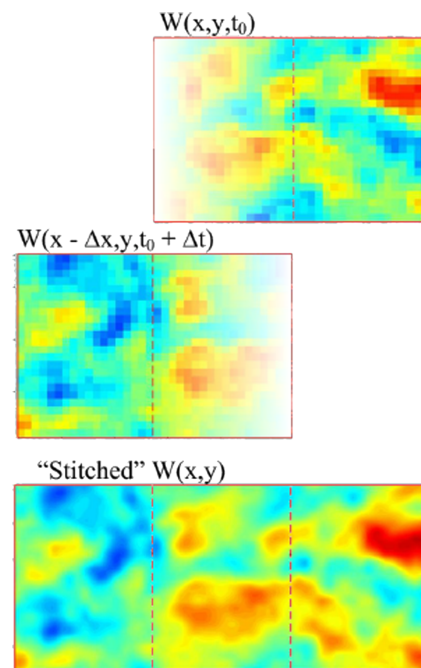

Fig. 1. Full stitching methodology (figure adopted from Ref. [14]).

B. Removing Mechanical Contamination

Mechanical contamination tends to cause beam path optics to rotate, which imposes non-turbulence related tip/tilt and piston on the laser beam encountering these optics. The tip/tilt and piston associated with mechanical contamination is indiscernible from the turbulence-induced components of these quantities. Therefore, all tip/tilt and pistons are initially removed from the wavefront measurements. It is worth noting that in extreme circumstances, mechanical contamination can also cause optics to deform, introducing higher-order disturbances into the laser beam. However, for all intents and purposes, the authors assume that mechanical contamination manifests only as tip/tilt and piston, as the higher-order disturbances associated with mechanical contamination are negligible. Furthermore, we assume that the higher-order disturbances imposed on the laser beam are entirely caused by optical turbulence. After removing the corrupted tip/tilt and piston from the wavefront measurements, the stitching method was used, which leverages these higher-order disturbances to reintroduce the turbulence-induced components of tip/tilt and piston. This algorithm was developed by Kemnetz [14,15]. To use the stitching method, two main assumptions are made. The first assumption requires that the measured wavefront aberrations are continuous in both space and time. This assumption means that stitching is not viable in environments where discontinuities such as shock waves or branch points are present. Second, the stitching method relies on the convective nature of the laser beam's aberrating structures. Therefore, the flow must be primarily convective. In addition to these assumptions, a sufficiently fast sampling rate must also be used to collect the wavefront measurements. The sampling rate is selected such that a sufficient overlap percentage exists between consecutive frames. By employing Taylor's frozen flow hypothesis [18], the measurement sample rate, f_s, and convective velocity, U_c, can be used to calculate the distance the optical turbulence structures are convected as $\Delta x = U_c (\frac{1}{f_s})$. Subsequently, the overlap percentage between adjacent frames is $(1 - \frac{\Delta x}{D}) \times 100$. If the assumptions defined above are valid, the overlap region between adjacent frames should contain the same phase. The tip/tilt and piston of the subsequent frame are then adjusted such that this stipulation is met.

Figure 1 visually describes how this procedure is conducted. The top figure represents a wavefront frame at instant t_0, and the middle figure represents wavefront frame at instant $t_0 + \Delta t$. Left of the dotted line in the top figure and right of the dotted line in the middle figure represent the overlap regions between these consecutive frames. After tip/tilt and piston of the wavefront frame at instant $t_0 + \Delta t$ are adjusted such that the tip/tilt and piston in the overlap regions of the wavefront frames at t_0 and $t_0 + \Delta t$ match, the overlap regions are blended together as shown in Fig. 1. The overlap regions are blended using a weighting function ranging linearly from zero to one for the wavefront frame at instant t_0 and from one to zero for the wavefront frame at instant $t_0 + \Delta t$. After blending the overlap regions, the wavefront frame at instant $t_0 + \Delta t$ is then added to the previous wavefront starting at the beginning of the overlap region of frame $t_0 + \Delta t$, as shown in the bottom plot of Fig. 1. As such, the non-overlap component of the frame is also added to the wavefront and will be used to stitch the next wavefront frame. As this process is repeated, a long wavefront strip is formed in the streamwise direction. To create a new time series of wavefronts now that tip/tilt and piston have been reintroduced, the so-called "variable aperture approach" can be applied [15]. This allows the stitched wavefront strip to be sampled for any streamwise aperture size, D, and sampling rate, f_s, by again enforcing Taylor's frozen flow hypothesis. The steps to perform stitching that are qualitatively described above are described in detail in Refs. [14,15].

The stitching method was used on all experimental wavefront measurements described in this work, which allowed the turbulence-induced component of tip/tilt and piston to be reintroduced into the wavefronts without the influence of mechanical contamination. The next sections describe the experimental setup and data processing procedures that allowed these wavefront measurements to be collected.

3. EXPERIMENTAL MEASUREMENTS

This section discusses the experimental setup and processing procedures required to measure and quantify atmospheric-imposed tilt. The experimental investigation was conducted using the AAOL. The experimental setups associated with both aircraft are described in detail. The processing procedure to convert measured slopes from the SHWFS to wavefronts is also described.

A. Airborne Aero-Optics Laboratory

The primary objective of AAOL is to provide an in-flight testing platform where aero-optics experiments can be performed under real conditions [9]. AAOL consists of two Falcon-10 aircraft capable of flying at varying separations, altitudes, and Mach numbers. For the experiments used in this research, one aircraft, designated as the source aircraft, projects a 532 [nm] diverging laser beam onto a custom-designed optical quality window mounted on the second aircraft, referred to here as the laboratory aircraft. The window is mounted in a specially designed aluminum frame, meant to limit distortions to the attached boundary layer as the air convects from the aircraft fuselage over the window [9]. The window has a clear aperture of 0.3048 [m] diameter, with optical quality of better than $\lambda/10$ in surface flatness.

For the experiments presented in this work, the two AAOL aircraft flew at the same altitude above ground level (AGL) such that the beam propagated through the atmosphere horizontally. This is significant because the horizontal propagation path allows us to assume that atmospheric optical turbulence strength remains fairly constant over the path. To collect SHWFS measurements at different altitudes, both aircraft climbed or descended to the same altitude to maintain horizontal propagation and the assumption of constant turbulence strength over the propagation range.

In addition to collecting data at different altitudes, SHWFS measurements were also collected of a beam that propagated over varying ranges. Large propagation ranges (accomplished by larger aircraft separations) as well as lower altitude flights impose greater optical distortions on the beam. Details pertaining to

the systems installed on both AAOL aircraft used to make these measurements are discussed in greater detail in the next sections.

1. AAOL: Source Aircraft

The source aircraft was equipped with a Laser Quantum Opus 532 [nm] 2 W laser, motorized system to vary beam divergence, a 50 [mm] diameter Optics in Motion 102 FSM, an AeroTech gimbal with a 100 [mm] mirror, a National Instruments PXI Real-Time system, a laptop for user control, and a GPS unit that allowed relative aircraft separations to be calculated in real time. This system allowed for both image-based and return-based tracking capability. The return signal came from the laser beam reflecting off a corner cube installed in the laboratory aircraft's acquisition window.
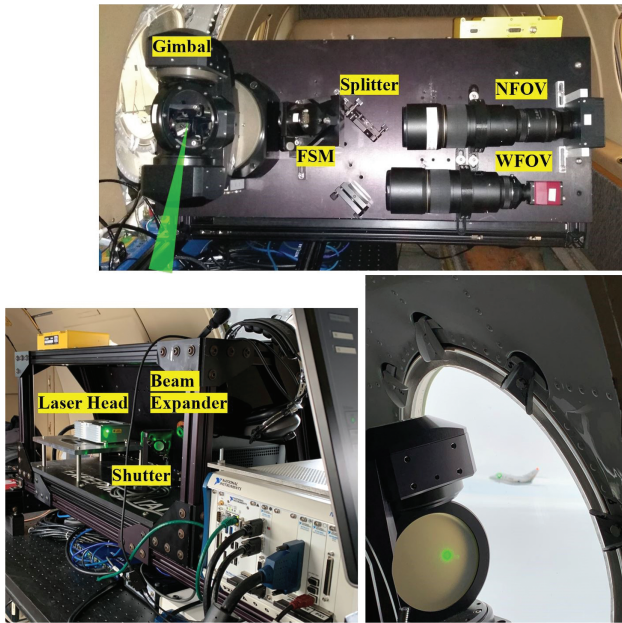

Fig. 2.   AAOL source aircraft setup [19].

Figure 2 illustrates the experimental setup in the source aircraft. A wide field of view (WFOV) camera with a 300 [mm] lens was used to locate the laboratory aircraft, and a narrow field of view (NFOV) camera with a 600 [mm] lens was used for tracking—either off the return signal or image features on the laboratory aircraft. Using the motorized beam divergence system, the divergence of the outgoing beam was changed by the user to sufficiently fill the acquisition window on the laboratory aircraft window regardless of the separation distance between aircraft [19,20].

2. AAOL: Laboratory Aircraft

The laboratory aircraft receives the incoming beam from the source aircraft and directs the beam to the SHWFS installed on a high-speed camera. Figure 3 illustrates the experimental setup of this aircraft. The beam enters through the optical quality window and is directed off a 0.3048 [m] flat steering mirror mounted on an AeroTech gimbal. To stabilize the incoming beam, a computer-controlled proportional feedback system was used. The gimbal forwards the beam through a Schmidt–Cassegrain telescope with a diameter of 203 [mm] and a central obscuration of 64 [mm] in diameter. A mirror is mounted on the back of the telescope's secondary mirror to pick off a portion of the beam for the tracking camera, which has a 500 [mm] focal length lens attached. After exiting the telescope, a portion of the beam is directed to an imaging camera, and the other portion of the beam is split again to be partitioned between an On-Trak PSM2-10 position sensing device (PSD) (which serves as a fine track system) as well as the SHWFS. The SHWFS has a spatial resolution of 50×50 subapertures 0.3 [mm] in size, allowing the wavefront distortions imposed on the beam to be measured with high spatial resolution [19,20]. The lenslet array of the SHWFS was mounted on a Phantom v1611 high-speed camera with a pixel size of 28 [μm].
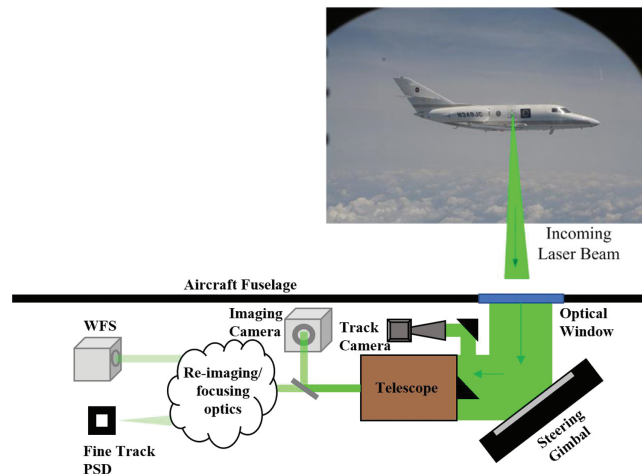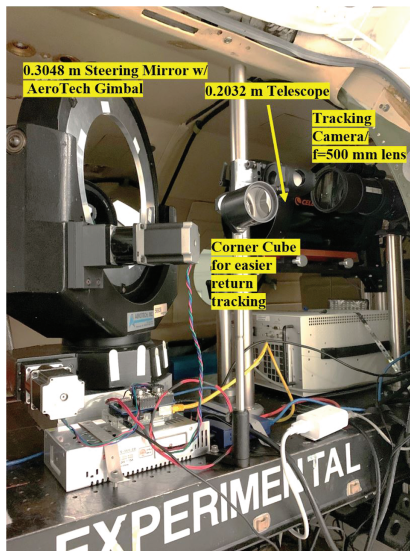

Fig. 3.   AAOL laboratory aircraft setup [19].

B. Data Collection Parameters

As discussed above, SHWFS measurements were collected at both varying altitudes and separations during two separate flight tests. Wavefronts were collected at 4 [kHz] with a varying, but sufficiently short exposure time (between 0.4 and 1 [μs]). The aircraft consistently flew at a cruise Mach number of 0.4, corresponding to a spatial overlap between consecutive wavefronts of approximately 83.5%. A total of 28,000 frames were collected per data point, resulting in approximately 7 [s] of wavefront measurements per data point. This corresponds to approximately 900 [m] of aircraft forward travel between the beginning and end of data collection. A sample rate of 4 [kHz] was selected to sufficiently resolve the range of relevant aberrating frequencies from higher-order disturbances to disturbances resulting from the large-scale optical turbulence structures in the atmosphere.

C. Processing Procedure

To convert the measured SHWFS centroids into usable wavefront measurements, various data processing steps needed to be employed. First, the subaperture centroids measured by the high-speed camera needed to be converted to slopes [21]. An algorithm identified areas of interest (AOIs) where the centroids were located, from which local slopes were calculated using the focal length of the lenslets. These slopes were converted into wavefronts using a least-squares reconstructor. Next, all tip/tilt and pistons as well as steady lensing were removed from the data. Steady lensing results from imperfect optics or temporally stationary wavefront disturbances. Since the stitching method relies on the convective nature of the wavefront's aberrating structures, it is required that steady lensing is removed. Finally, the stitching method, described in Section 2.B, was then used to reintroduce the turbulence-induced component of tip/tilt and piston back into the wavefronts.

It should also be noted that in addition to propagating through the atmosphere, the laser beam projected from the source aircraft to the laboratory aircraft also propagated through the aero-optical environment in proximity of the laboratory aircraft. Since the boundary layer thickness of the aircraft is approximately 50 [mm], which is significantly smaller than the measurement aperture ($D = 0.2$ [m]), we can assert with confidence that the aero-optical environment of the laboratory aircraft introduced negligible tip/tilt into the laser beam [14]. In other words, the tip/tilt and piston reintroduced into the wavefronts using the stitching method was primarily tip/tilt and piston resulting from atmospheric optical-turbulence-related disturbances.

4. RESULTS AND DISCUSSION

Using the processing procedures described in Section 3.C coupled with the stitching method discussed in Section 2.B, atmospheric-imposed tilt was quantified from the measured wavefronts. The measured root-mean-square tilt results, $\theta_{x,\text{RMS}}$, for data collected at varying aircraft separations and altitudes are shown in Fig. 4.

In this plot, the x axis represents the propagation distance, Z, and the y axis represents the root-mean-square tilt, $\theta_{x,\text{RMS}}$,
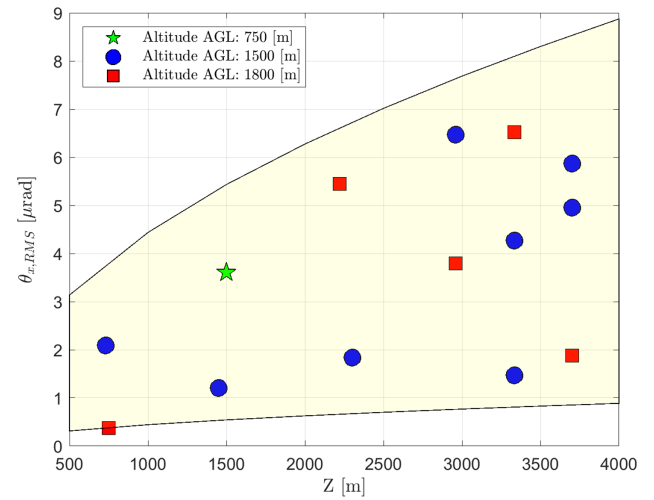

Fig. 4. Measured atmospheric root-mean-square tilt resultant from atmospheric propagation. The yellow region represents the $\theta_{x,\text{RMS}}$ values expected for C_n^2 environments between 1×10^{-16} and 1×10^{-14} [m$^{-2/3}$].

imposed on the laser beam by the atmosphere. The different markers indicate the altitudes AGL at which data were collected. Atmospheric optical turbulence strength is usually quantified in terms of the index-of-refraction structure constant, C_n^2. The shaded yellow region in the figure represents the root-mean-square tilt, $\theta_{x,\text{RMS}}$, values expected for C_n^2 values between 1×10^{-16} and 1×10^{-14} [m$^{-2/3}$], which are reasonable given the aircraft altitudes when data collection took place. This was calculated using

$$\theta_{\text{RMS}} = \sqrt{0.182\left(\frac{\lambda}{D}\right)^2 \left\{\frac{D}{3.0[C_n^2 Z(\frac{2\pi}{\lambda})^2]^{-3/5}}\right\}^{5/3}}, \quad \textbf{(6)}$$

where λ is the laser wavelength, D is the aperture diameter, and Z is the laser propagation distance [2]. In this equation, we assume that the beam was propagating as a spherical wave and that C_n^2 remains constant along the propagation path. The measured root-mean-square tilt values are in agreement with those expected for realistic C_n^2 environments.

Power spectral densities were calculated from the stitched atmospheric tilt time series. The results are shown in Fig. 5 where the black line represents the experimentally measured atmospheric tilt power spectrum. The top figure represents a tilt power spectrum calculated from wavefront measurements collected in a low atmospheric optical turbulence strength environment ($C_n^2 = 9.6 \times 10^{-17}$ [m$^{-2/3}$]). The bottom left and right figures represent tilt power spectra calculated from wavefront measurements collected in a medium ($C_n^2 = 5.9 \times 10^{-16}$ [m$^{-2/3}$]) and high ($C_n^2 = 1.3 \times 10^{-15}$ [m$^{-2/3}$]) atmospheric optical turbulence strength environments, respectively. The analytic solution to the single axis Z-tilt power spectral density, $\Phi_Z(f)$, for a spherical wave propagating through the atmosphere can be found in Refs. [22,23] and is given by
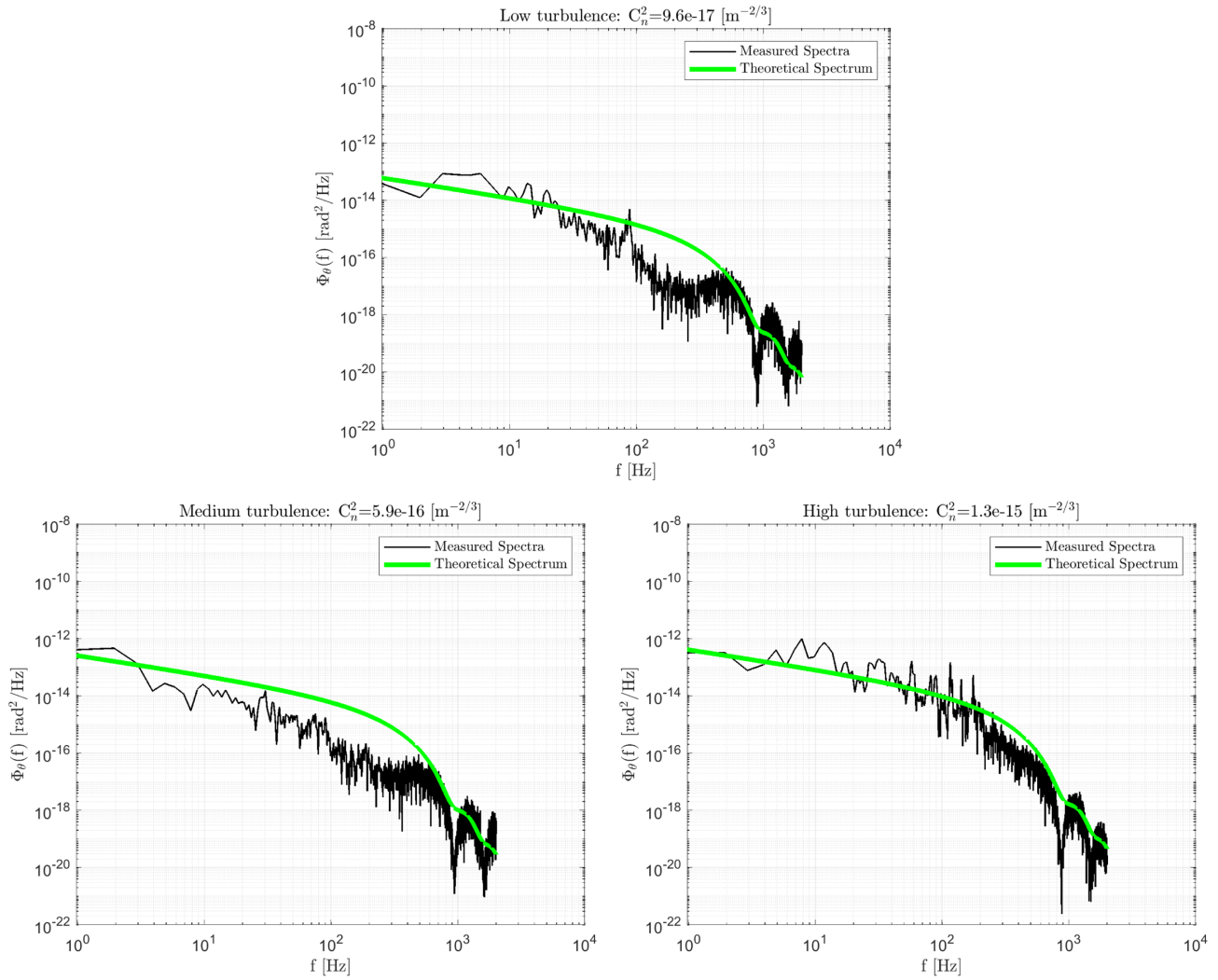
Fig. 5. Experimentally measured tilt power spectra for low (top), medium (bottom left), and high (bottom right) atmospheric turbulence strength environments.

$$\Phi_Z(f) = 0.503 D^{-4} f^{-14/3} \int_0^Z \left(C_n^2(z) U_c(z)^{11/3} (1 - z/Z)^{-2} \right.$$

$$\left. \times \left[\int_0^1 x^{11/3} (1 - x^2)^{1/2} J_2^2 \left(\frac{\pi f (1 - z/Z) D}{U_c(z)} \right) dx \right] \right) dz, \tag{7}$$

where z is the position along the path, Z is the total propagation distance, U_c is convective velocity, D is the measurement aperture diameter, and J_2 is the Bessel function of the first kind. The experimental measurements made use of a 0.2 [m] aperture and propagation distance, or range was determined from the aircraft separation when the wavefront measurements were collected. The C_n^2 values used in Eq. (7) were determined using higher-order disturbances from the wavefront measurements. Specifically, wavefront slope discrepancy was used to calculate the atmospheric coherence length, r_0, from which C_n^2 could be estimated for each of the measured data points [19,20,24,25]. More detail on how C_n^2 was estimated from the SHWFS measurements collected in-flight can be found in Refs. [19,20]. The

resultant analytic tilt power spectrum calculated using Eq. (7) is represented in the plots with a green line.

In Fig. 5, it can be seen that the analytic power spectral densities for atmospheric tilt match the experimental results well. This provides validation that the stitching algorithm was effective at reconstructing atmospheric tilt from the measured wavefronts. For the high optical turbulence strength case ($C_n^2 = 1.3 \times 10^{-15}$ [m$^{-2/3}$]) shown in the bottom right plot of Fig. 5, the experimentally measured power spectrum is in agreement with theory for the entire measured spectrum. Since the analytic solution to the tilt power spectral density assumes Kolmogorov turbulence, the agreement between the analytic tilt power spectral density and the measured result indicates that in this case, the turbulence environment through which the beam propagated had Kolmogorov-like behavior. For the low and medium optical turbulence strength cases ($C_n^2 = 9.6 \times 10^{-17}$ and $C_n^2 = 5.9 \times 10^{-16}$ [m$^{-2/3}$], respectively), the agreement between the experimentally measured and analytic tilt power spectra is particularly good at the low- and high-frequency ends of the spectrum. The middle frequencies (between 100 and 500 [Hz]) are less energetic than what the analytic power spectrum

predicts. One potential explanation for the lower-than-expected energy at intermediate frequencies may be that the atmospheric turbulence environment where these data were collected had a slight deviation from a Kolmogorov description. Another possible explanation is that the improved signal (atmospheric higher-order optical disturbances) to noise (other types of measured disturbances) associated with higher C_n^2 environments improves results. In Fig. 5, it can be seen that as the strength of the atmospheric optical turbulence environment increases, the energy associated with the middle frequencies more closely matches the analytic solution. The definitive reasoning for the lower-than-expected spectral power at the intermediate frequencies for the low and medium atmospheric optical turbulence strength cases is still being investigated.

Also noticed in the high-frequency end of the spectra for all cases are dropouts, or frequencies with comparatively low energy. For particular structure sizes, the period of the turbulence structure relative to the size of the aperture causes minimal Z-tilt. The dropouts in the measured tilt power spectral density at approximately 900 and 1600 [Hz] are resultant from these Z-tilt extinction frequencies and are predicted in literature [14,15,17].

As evident in the tilt power spectral density results presented above, the stitching method effectively reintroduced turbulence-induced tilt imposed by the atmosphere. Once the full stitching method is used to create a long wavefront strip, any size streamwise aperture and sampling rate can be used to re-sample the wavefronts using the variable aperture approach, as described earlier [15]. Therefore, a wavefront strip that is $N_y \times N_x$ can be sampled to $N_y \times N_D$ in a manner that replicates imposing a convective velocity. Here, N_D represents the number of points across the aperture in the streamwise direction. It is important to note that the aperture size in the spanwise direction remains the same as the measurement aperture size (in this case, $D = 0.2$ [m]). However, the aperture size in the streamwise or stitched direction can be varied. As an example, consider re-sampling the stitched wavefront strip using a square, $N_y \times N_y$, aperture. If the convective velocity, U_c, is 135 [m/s] and we define the sampling rate, f_s, to be 10,000 [Hz], the associated convective distance between adjacent frames would be $\Delta x = U_c(\frac{1}{f_s}) = 0.0135$ [m]. Therefore, the next $N_y \times N_y$ wavefront frame would be located 0.0135 [m] further in the streamwise direction along the long strip. This is visually represented in Fig. 6.

Here, the black square represents the first $N_y \times N_y$ wavefront frame, and the subsequent gray squares represent $N_y \times N_y$
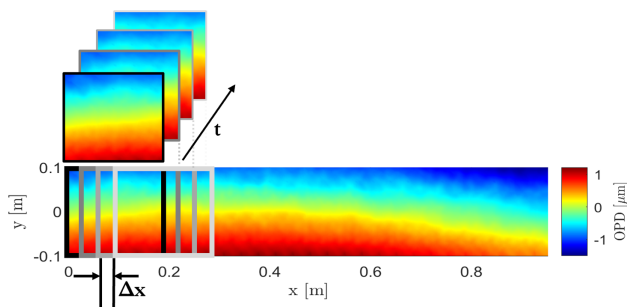

Fig. 6. Sampling of a long wavefront strip where the boxes represent re-sampled wavefront frames.

wavefront frames at later time steps. This is repeated until the end of the long wavefront strip is reached. The new wavefront time series now formed includes the turbulence-induced component of tip/tilt and piston initially removed from the measurements and is no longer susceptible to streamwise aperture effects. In other words, the resultant OPD_{RMS} of the wavefront time series with tip/tilt and piston should be invariant with aperture size. To validate this, using the variable aperture approach, various aperture sizes were imposed on the stitched wavefront strip, and the OPD_{RMS} associated with each aperture size was calculated. This procedure was repeated for all measured data points. To generalize the results, for each data point, the mean OPD_{RMS} calculated over all aperture sizes ($\overline{OPD_{RMS}(D)}$) was removed. Removing the mean OPD_{RMS} for each data point eliminates the dependence on the atmospheric optical turbulence strength environment that the beam propagated through. These results were ensemble averaged over all data collected, and the results are shown in Fig. 7.

In this plot, the x axis represents aperture size, D, and the y axis represents $OPD_{RMS}(D) - \overline{OPD_{RMS}(D)}$. In other words, the y axis represents the deviation of OPD_{RMS} as a function of aperture size from the expected OPD_{RMS} for each data collection. Aperture sizes from 0.02 to 15 [m] were used to re-sample the stitched wavefront time series. Despite small deviations, OPD_{RMS} of the wavefront time series with tip/tilt and piston reintroduced remains fairly constant (deviations less than 0.1 [μm]) with aperture size, verifying the functionality of the algorithm.

To further emphasize the utility of the results presented in this paper, it is important to understand the effect of aperture size on wavefront measurements. The size of the measurement aperture acts as a form of spatial filter, where optical turbulence structures of the order of the aperture size and larger manifest as tip/tilt and piston in the wavefront measurements, and optical turbulence structures smaller than the aperture manifest as higher-order disturbances in the wavefront measurements. As shown above, once tip/tilt and piston are reintroduced into the wavefronts and a wavefront strip is formed using the stitching method, any sampling rate and aperture size can be used to re-sample the wavefront strip to form a new time series. Therefore,
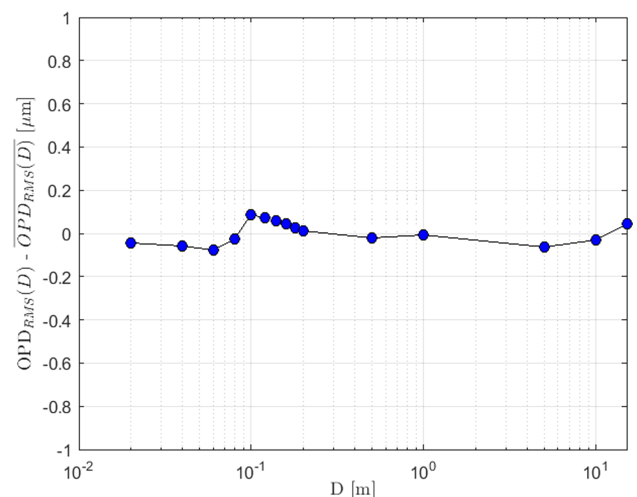

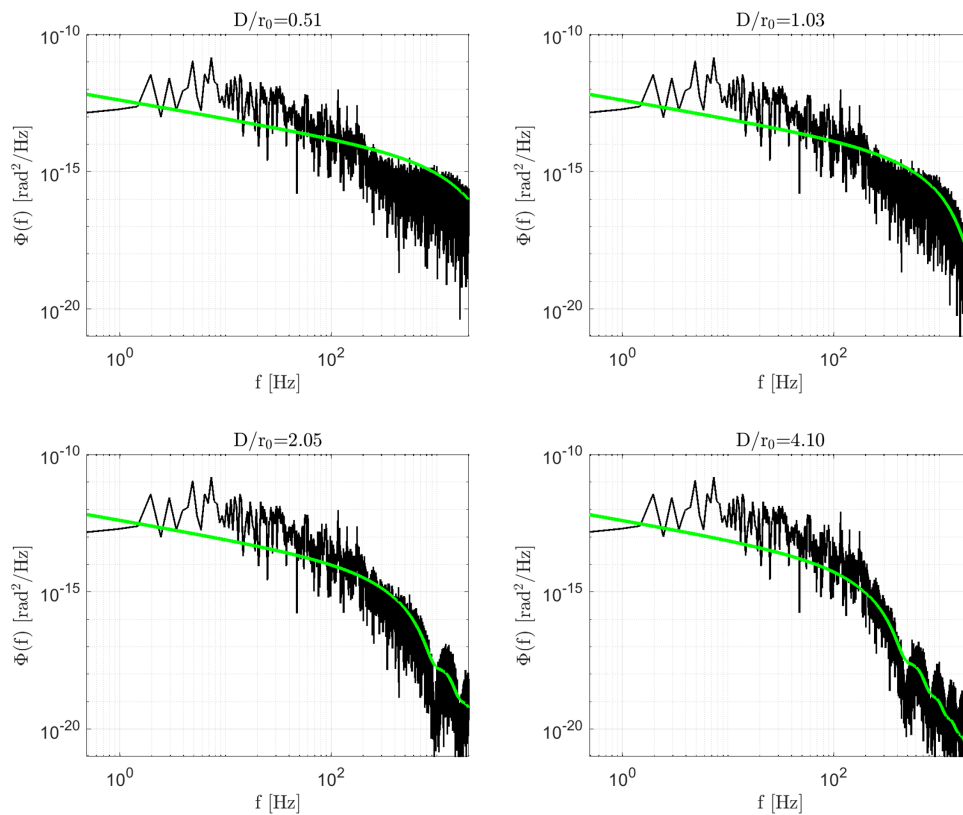**Fig. 7.** OPD_{RMS} as a function of aperture size for the stitched wavefronts.

Fig. 8. Experimental atmospheric tilt power spectral density re-sampled for varying aperture sizes: (top left) $D/r_0 = 0.51$, (top right) $D/r_0 = 1.03$, (bottom left) $D/r_0 = 2.05$, and (bottom right) $D/r_0 = 4.10$.

by re-sampling the wavefront strip using varying streamwise aperture sizes, the amplitude and frequency of measured tilt changes. To demonstrate this, a stitched wavefront strip was re-sampled for varying streamwise aperture sizes normalized by the atmospheric coherence length, r_0. The normalized aperture sizes used were $D/r_0 = 0.51$, 1.03, 2.05, and 4.10. Z-tilt was calculated from these new wavefront times series, and power spectral densities were computed for each case. These results are presented in Fig. 8. Analytic tilt power spectral densities were also calculated for the varying aperture sizes using Eq. (7) and are represented in the plots with a green line. Similar to above, the r_0 values obtained for this analysis were calculated using wavefront slope discrepancy [19,20,24,25]. Subsequently, r_0 was used to calculate C_n^2, which was then used in Eq. (7).

It can be seen that the experimental atmospheric tilt power spectral densities for wavefronts re-sampled using varying aperture sizes are in agreement with the analytic solutions. For the smallest aperture case, $D/r_0 = 0.51$, notice that significantly more energy exists in the high-frequency end of the spectrum compared to the largest aperture case, $D/r_0 = 4.10$. As aperture size increases, optical turbulence disturbances transition from manifesting as tip/tilt and piston to becoming higher-order disturbances. For the largest aperture case of $D/r_0 = 4.10$, not only does significantly less energy exist in the high-frequency end of the spectrum, but more Z-tilt extinction frequencies are noticed in both the analytic solution and experimental results.

5. CONCLUSION

The goal of this work was to experimentally quantify the tilt imposed on a continuous laser beam by the atmosphere using SHWFS measurements. The beam was propagated between two aircraft flying at varying separations and altitudes. Until recently, the in-flight measurement of atmospheric-imposed tilt was not possible since mechanical contamination also manifests as tip/tilt in the measured wavefronts. An algorithm referred to as the stitching method was recently developed that restores the turbulence-induced component of tip/tilt and piston without the influence of mechanical disturbances. Once stitching was used, the resultant root-mean-square tilt associated with the atmospheric disturbances was quantified. These results were shown to agree with theoretical predictions. This is the first time that atmospheric tilt was experimentally measured in-flight. Power spectral densities were calculated for the experimentally measured atmospheric tilt time series. It was shown that the experimentally measured power spectra were in agreement with the analytic solution. This result confirmed that the stitching method was effective at reconstructing atmospheric tilt from the measured wavefronts. Additionally, the slope of the spectra is in agreement with theory confirming the Kolmogorov-like behavior of turbulence where the wavefronts were measured. Future papers will discuss validation of the stitching method for reconstructing atmospheric tilt from wavefront measurements as well as provide a detailed error analysis to further support the results presented in this paper.

REFERENCES

1. E. J. Jumper and E. J. Fitzgerald, "Recent advances in aero-optics," Prog. Aerosp. Sci. **37**, 299–339 (2001).
2. G. A. Tyler, "Bandwidth considerations for tracking through turbulence," J. Opt. Soc. Am. A **11**, 358–367 (1994).
3. S. Gordeyev and E. Jumper, "Fluid dynamics and aero-optics of turrets," Prog. Aerosp. Sci. **46**, 388–400 (2010).
4. E. J. Jumper, M. Zenk, S. Gordeyev, D. Cavalieri, and M. R. Whiteley, "The airborne aero-optics laboratory, AAOL," Proc. SPIE **8395**, 839507 (2012).
5. N. De Lucca, S. Gordeyev, and E. Jumper, "The airborne aero-optics laboratory, recent data," Proc. SPIE **8395**, 839508 (2012).
6. T. J. Brennan and D. J. Wittich, "Statistical analysis of airborne aero-optical laboratory optical wavefront measurements," Opt. Eng. **52**, 071416 (2013).
7. C. Porter, S. Gordeyev, M. Zenk, and E. Jumper, "Flight measurements of the aero-optical environment around a flat-windowed turret," AIAA J. **51**, 1394–1403 (2013).
8. M. J. Krizo, S. J. Cusumano, S. T. Fiorino, R. Heap, V. Velten, J. Brown, and R. J. Bartell, "Design, development, and in-flight testing of a pointer/tracker for in-flight experiments to measure aero-optical effects over a scaled turret," Opt. Eng. **52**, 071415 (2013).
9. M. Kalensky, S. Gordeyev, and E. J. Jumper, "In-flight studies of aero-optical distortions around AAOL-BC," in *Aviation Forum* (American Institute of Aeronautics and Astronautics, 2019).
10. S. Gordeyev and M. Kalensky, "Effects of engine acoustic waves on aerooptical environment in subsonic flight," AIAA J. **58**, 5306–5317 (2020).
11. M. Kalensky, J. Wells, and S. Gordeyev, "Image degradation due to different in-flight aero-optical environments," Opt. Eng. **59**, 104104 (2020).
12. Y. Diskin, M. Whiteley, M. Grose, K. Jackovitz, R. Drye, B. Hampshire, M. Owens, E. Smith, E. Magee, M. Kalensky, E. Jumper, S. Gordeyev, and A. Archibald, "Aircraft to ground profiling: turbulence measurements and optical system performance modeling," AIAA J. **59**, 4610–4625 (2021).
13. P. H. Merritt and M. F. Spencer, *Beam Control for Laser Systems*, 2nd ed. (Directed Energy Professional Society, 2018).
14. M. Kemnetz, "Analysis of the aero-optical component of the jitter using the stitching method," Ph.D. thesis (University of Notre Dame, 2019).
15. M. R. Kemnetz and S. Gordeyev, "Analysis of aero-optical jitter in convective turbulent flows using stitching method," AIAA J. **60**, 14–30 (2021).
16. E. J. Jumper and S. Gordeyev, "Physics and measurement of aero-optical effects: past and present," Annu. Rev. Fluid Mech. **49**, 419–441 (2017).
17. J. P. Siegenthaler, "Guidelines for adaptive-optic correction based on aperture filtration," Ph.D. thesis (University of Notre Dame, 2008).
18. G. I. Taylor, "The spectrum of turbulence," Proc. R. Soc. A **164**, 476–490 (1938).
19. M. Kalensky, E. J. Jumper, and S. Gordeyev, "Extracting atmospheric optical turbulence parameters from AAOL-BC wavefront measurements," in *AIAA SCITECH Forum* (American Institute of Aeronautics and Astronautics, 2022).
20. M. Kalensky, "Airborne measurement of atmospheric-induced beam jitter," Ph.D. thesis (University of Notre Dame, 2022).
21. A. M. Nightingale and S. Gordeyev, "Shack-Hartmann wavefront sensor image analysis: a comparison of centroiding methods and image-processing techniques," Opt. Eng. **52**, 071413 (2013).
22. V. Vaughn, "The power spectra for g-tilt and z-tilt," Tech. Rep. (Optical Sciences, 1996).
23. P. Merritt, *Beam Control for Laser Systems* (Directed Energy Professional Society, 2012).
24. T. J. Brennan, "Anatomy of the slope discrepancy structure function: characterization of turbulence," Proc. SPIE **5087**, 103–114 (2003).
25. T. Brennan, "Estimation of atmospheric parameters from the slope discrepancy," Tech. Rep. (Optical Sciences, 2003).